
Per-channel autoregressive linear prediction padding in tiled CNN processing of 2D spatial data

Olli Niemitalo 

HAMK Häme University of Applied Sciences
Hämeenlinna, Finland
Olli.Niemitalo@hamk.fi

Otto Rosenberg 

HAMK Häme University of Applied Sciences
Hämeenlinna, Finland
Otto.Rosenberg@hamk.fi

Nathaniel Narra 

HAMK Häme University of Applied Sciences
Hämeenlinna, Finland
Nathaniel.Narra@hamk.fi

Olli Koskela 

HAMK Häme University of Applied Sciences
Hämeenlinna, Finland
Olli.Koskela@hamk.fi

Iivari Kunttu 

HAMK Häme University of Applied Sciences
Hämeenlinna, Finland
Iivari.Kunttu@hamk.fi

Abstract

We present linear prediction as a differentiable padding method. For each channel, a stochastic autoregressive linear model is fitted to the padding input by minimizing its noise terms in the least-squares sense. The padding is formed from the expected values of the autoregressive model given the known pixels. We trained the convolutional RVSR super-resolution model from scratch on satellite image data, using different padding methods. Linear prediction padding slightly reduced the mean square super-resolution error compared to zero and replication padding, with a moderate increase in time cost. Linear prediction padding better approximated satellite image data and RVSR feature map data. With zero padding, RVSR appeared to use more of its capacity to compensate for the high approximation error. Cropping the network output by a few pixels reduced the super-resolution error and the effect of the choice of padding method on the error, favoring output cropping with the faster replication and zero padding methods, for the studied workload.

1 Introduction

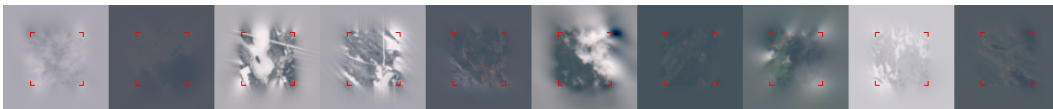


Figure 1: Satellite images padded using our linear prediction padding method (variant 1p6x7).

Geospatial rasters and other extensive spatial data can be processed in tiles (patches) to work around memory limitations. The results are seamless if all whole-pixel shifts of the tiling grid result in the same stitched results. A convolutional neural network (CNN) consisting of valid convolutions and pointwise operations is equivariant to whole-pixel shifts. In such *shift equivariant* CNN-based processing, each input tile must cover the receptive fields of the output pixels, *i.e.* input tiles must

be overlapped. This wastefully repeats computations. In deep CNNs, the receptive fields may be thousands of pixels wide (Araujo et al. 2019), exacerbating the problem.

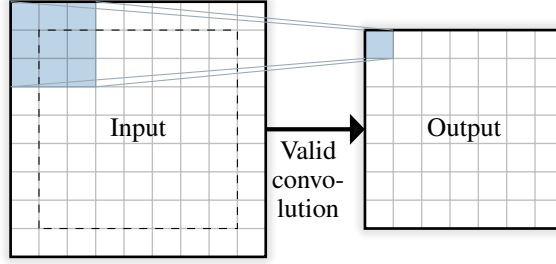


Figure 2: Valid convolution with a 3×3 kernel with origin in the middle erodes data spatially by a one-pixel-thick layer at each image edge. The receptive field of a single output pixel (■) is illustrated.

Spatial reduction (see Fig. 2) in deep CNNs is commonly compensated for by padding the input of each spatial convolution, with zeros in the case of the typically used *zero padding* (`zero` for brevity) or with the value of the nearest input pixel in *replication padding* (`repl`). In the less used polynomial *extrapolation padding* (`extrN`), a Lagrange polynomial of a degree $N - 1$ is fitted to the N nearest input pixels from the same row or column, and the padding is sampled from the extrapolated polynomial. `extr0` is equivalent to `zero` and `extr1` to `repl`.

An ideal padding method would exactly predict the spatial data outside the padding input view. This is not possible to do for data coming from an effectively random process, such as natural data or a CNN feature map derived from it. Using padding increases processing error towards tile edges (Huang et al. 2018) and will generally break CNN shift equivariance. Center-cropping the CNN output reduces the error (Huang et al. 2018) and thus indirectly improves shift equivariance. The strength of the receptive fields of output neurons typically decay super-exponentially with distance to their center (Luo et al. 2016), meaning that an output center crop less than the radius of the theoretical receptive field could reduce the processing error close to that of a valid-convolution CNN.

In this work we introduce *linear prediction padding* (abbreviated `lp`, see Fig. 1) and evaluate the performance of tiled CNN super-resolution employing padding methods `lp`, `zero`, `repl`, and `extr`.

2 Linear prediction padding

Linear prediction is a method for recursively predicting data using nearby known or already predicted data as input (for an introduction, see Makhoul 1975 for the 1D case and Weinlich 2022 for the 2D case, both very approachable texts). Linear prediction is closely related to stochastic autoregressive (AR) processes. In the 2D case, we can model single-channel image or feature map data I , assumed real-valued, by a zero-mean stationary process \hat{I} :

$$\hat{I}_{(y,x)+h_0} = \sum_{i=1}^P a_i \hat{I}_{(y,x)+h_i} + \varepsilon_{(y,x)+h_0}, \quad (1)$$

where (y, x) are integer spatial coordinates, a_i are coefficients that parameterize the process, ε is zero-mean independent and identically distributed (IID) noise, and the *extended neighborhood* h is a list of 2D coordinate offsets (relative to a shared origin), first the pixel of interest $\hat{I}_{(y,x)+h_0}$, followed by its *neighborhood* $\hat{I}_{(y,x)+h_1 \dots P}$ in any order. Each pixel depends linearly on P neighbors (see Fig. 3). Our approach to linear prediction padding is to least-squares (LS) fit the AR model (Eq. 1) to actual image data I and to compute the padding as conditional expectancies assuming that the data obeys the model, $\hat{I} = I$.

The LS fit is obtained by minimizing the mean square prediction error (MSE), with residual noise as the error:

$$\varepsilon_{(y,x)+h_0} = \sum_{i=1}^P a_i I_{(y,x)+h_i} - I_{(y,x)+h_0}, \quad \text{MSE} = \frac{1}{|S|} \sum_{(y,x) \in S} \left(\sum_{i=1}^P a_i I_{(y,x)+h_i} - I_{(y,x)+h_0} \right)^2, \quad (2)$$

$$S = \{(y, x) \mid (y, x) + h_i \in K \text{ for all } i \in [0, P]\}$$

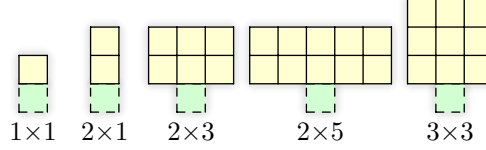


Figure 3: Illustration of some rectangular 2D neighborhoods (with pixels \square) next to the pixel of interest (\boxplus), defining the linear dependency structure of a downwards causal AR model. The extended neighborhood 1×1 can be defined by $h = [(1, 0), (0, 0)]$ and 2×1 by $h = [(2, 0), (0, 0), (1, 0)]$.

where S is the set of coordinates that keeps all pixel accesses in the sums within the set of input image pixel coordinates K (see the left side of Fig. 4).

The noise, being zero-mean by definition, does not contribute to the AR process expected value:

$$\mathbb{E}(\hat{I}_{(y,x)+h_0}) = \mathbb{E}\left(\sum_{i=1}^P a_i \hat{I}_{(y,x)+h_i} + \varepsilon_{(y,x)+h_0}\right) = \sum_{i=1}^P a_i \mathbb{E}(\hat{I}_{(y,x)+h_i}) + 0. \quad (3)$$

We can recursively calculate conditional expectances (the padding) further away from K using both the known pixels (the input image) and any already calculated expectances (the nascent padding):

$$\mathbb{E}(\hat{I}_{(y,x)+h_0} \mid \hat{I}_{(y,x) \in K}) = \sum_{i=1}^P a_i \begin{cases} \hat{I}_{(y,x)+h_i} & \text{if } (y,x)+h_i \in K, \\ \mathbb{E}(\hat{I}_{(y,x)+h_i} \mid \hat{I}_{(y,x) \in K}) & \text{otherwise.} \end{cases} \quad (4)$$

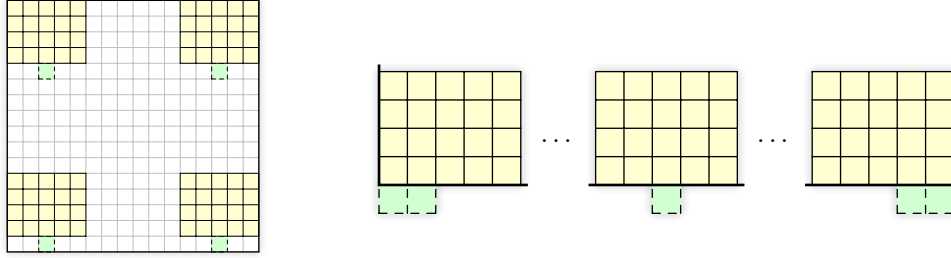


Figure 4: Downwards linear prediction padding with a 4×5 neighborhood — Left: predicted (\boxplus) and neighborhood pixels (\square) at the corners of the rectangular area of coordinates over which MSE is calculated during fitting. Right: corner handling prevents narrowing of the recursive prediction front.

We use rotated extended neighborhoods to pad in different directions, and adjust the extended neighborhoods (see the right side of Fig. 4) when padding near the corners. We pad channels of multi-channel data separately. Before padding, we make the data zero-mean by mean subtraction, which we found necessary for numerically stable Cholesky solves of AR coefficients and to meet the assumption of a zero-mean AR process. We add the mean back after padding. Depending on the extended neighborhood shape, we use a method based on covariance or a method based on autocorrelation.

2.1 Covariance method

For one ($P = 1$) and two-pixel ($P = 2$) neighborhoods, the error to minimize can be expressed using the shorthand r_{ij} for the means of products that are elements of a *covariance matrix* r :

$$P=1: \quad \text{MSE} = \frac{1}{|S|} \sum_{(y,x) \in S} (a_1 I_{(y,x)+h_1} - I_{(y,x)+h_0})^2 = a_1^2 r_{11} - 2a_1 r_{01} + r_{00}$$

$$P=2: \quad \text{MSE} = \frac{1}{|S|} \sum_{(y,x) \in S} (a_1 I_{(y,x)+h_1} + a_2 I_{(y,x)+h_2} - I_{(y,x)+h_0})^2 \quad (5)$$

$$= a_1^2 r_{11} + 2a_1 a_2 r_{12} - 2a_1 r_{01} + a_2^2 r_{22} - 2a_2 r_{02} + r_{00},$$

$$\text{where } r_{ij} = \frac{1}{|S|} \sum_{(y,x) \in S} I_{(y,x)+h_i} I_{(y,x)+h_j}, \quad r_{ij} = r_{ji}. \quad (6)$$

The LS solutions can be found by solving what are known as the *normal equations*:

$$\begin{aligned}
 P=1 : \quad \frac{\partial \text{MSE}}{\partial a_1} &= 2a_1 r_{11} - 2r_{01} = 0 & \Rightarrow & \quad a_1 = \frac{r_{01}}{r_{11}} \\
 P=2 : \quad \begin{cases} \frac{\partial \text{MSE}}{\partial a_1} = 2a_1 r_{11} + 2a_2 r_{12} - 2r_{01} = 0 \\ \frac{\partial \text{MSE}}{\partial a_2} = 2a_1 r_{12} + 2a_2 r_{22} - 2r_{02} = 0 \end{cases} & \Rightarrow & \begin{cases} a_1 = \frac{r_{01} r_{22} - r_{02} r_{12}}{r_{11} r_{22} - r_{12}^2} \\ a_2 = \frac{r_{02} r_{11} - r_{01} r_{12}}{r_{11} r_{22} - r_{12}^2} \end{cases} \quad (7)
 \end{aligned}$$

In implementation, we used a safe version of the division operator and its derivatives that replaces infinities with zeros in results. For any P , the normal equations involve the covariance matrix r :

$$\begin{bmatrix} r_{11} & r_{12} & \dots & r_{1P} \\ r_{12} & r_{22} & \dots & r_{2P} \\ \vdots & \vdots & \ddots & \vdots \\ r_{1P} & r_{2P} & \dots & r_{PP} \end{bmatrix} \begin{bmatrix} a_1 \\ a_2 \\ \vdots \\ a_P \end{bmatrix} = \begin{bmatrix} r_{01} \\ r_{02} \\ \vdots \\ r_{0P} \end{bmatrix}. \quad (8)$$

The approach is known as the *covariance method*. We implemented it only for the neighborhoods 1×1 (method `1p1x1cs` where `cs` stands for covariance, stabilized) and 2×1 (`1p2x1cs`), using Eq. 7 and stabilization of the effectively 1D linear predictors by reciprocating the magnitude of each below-unity-magnitude root of the AR process characteristic polynomial of lag operator B and by obtaining the coefficients from the expanded manipulated polynomial (see Appendix A for details):

$$1 \times 1 : \quad 1 - a_1 B, \quad 2 \times 1 : \quad 1 - a_1 B - a_2 B^2. \quad (9)$$

2.2 Autocorrelation method with Tukey window and zero padding

For methods `1p2x1`, `1p2x3`, `1p2x5`, `1p3x3`, `1p4x5`, and `1p6x7`, named by the height \times width of the neighborhood in vertical padding, we redefined r_{ij} as normalized (N_y, N_x) -periodic autocorrelation:

$$r_{ij} = \frac{R_{h_i - h_j}}{N_y N_x}, \quad R_{(\Delta y, \Delta x)} = \sum_{y=0}^{N_y-1} \sum_{x=0}^{N_x-1} I_{(y,x)} I_{((y-\Delta y) \bmod N_y, (x-\Delta x) \bmod N_x)}. \quad (10)$$

To reduce periodization artifacts, for use in Eq. 10, we multiplied the image horizontally and vertically by a Tukey window with a constant segment length of 50% and zero padded it sufficiently to prevent wraparound. For `1p2x5`, `1p3x3`, `1p4x5`, and `1p6x7` we accelerated calculation of R using fast Fourier transforms (FFTs) taking advantage of the Wiener–Khinchin theorem, $R = \text{IDFT2}(|\text{DFT2}(I)|^2)$ for our purposes, where DFT2 and IDFT2 are the 2D discrete Fourier transform and its inverse.

2.3 Implementation

We implemented linear prediction padding in the JAX framework (Bradbury et al. 2025) and solved Eq. 8 using a differentiable Cholesky solver from Lineax (Rader et al. 2023), stabilizing solves by adding a small constant 10^{-7} to diagonal elements of the covariance matrix, *i.e.* by ridge regression.

While not dictated by the theory, we constrained our implementation to rectangular neighborhoods (as in Fig. 3) with the predicted pixel located adjacent to and centered on the neighborhood with the exception of corner padding (see Fig. 4). Our implementation benefited from the capability of JAX to 1) *scan* the recursion for paddings larger than a 1-pixel layer, 2) to *vmap* (vectorizing map) for parallelization of the padding front and for calculations over axes of rectangular unions of extended neighborhoods including corner handling variants, and 3) to fuse convolution with covariance statistics collection. As far as the authors are aware, such automated fusing would not take place in PyTorch that at present only offers an optimized computational kernel for zero padding.

3 Evaluation in RVSR super-resolution

We reimplemented the convolutional RVSR $4 \times$ super-resolution model (Conde et al. 2024) in JAX-based Equinox (Kidger and Garcia 2021) with a fully configurable padding method (see Fig. 5) and trained its 218 928 training-time parameters from scratch using MSE loss. For some experiments, to emulate network output center cropping, we omitted padding from the inputs of a number of the last conv layers and cropped the bilinear upscale. We define *output crop* as the number of 4-pixels-thick

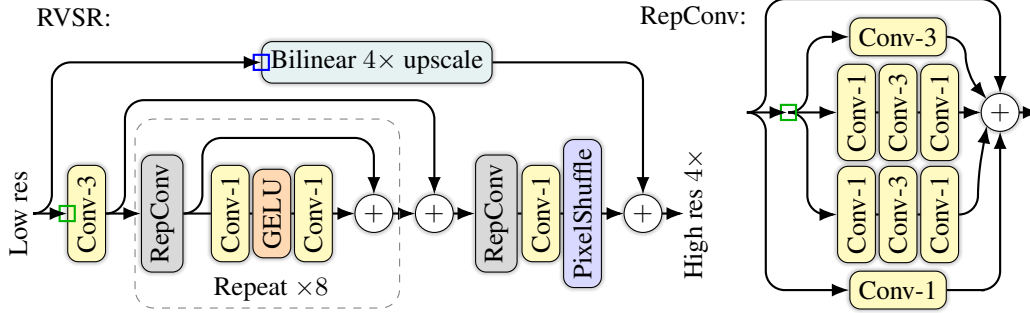


Figure 5: The convolutional RVSR super-resolution model. The spatial sizes of convolution kernels were $N \times N$ for Conv- N . Bilinear image upscaling methods in JAX and PyTorch implicitly replication pad their inputs. We padded upscale input explicitly (□) with the method configurable separately from padding of Conv inputs (◻). The RepConv block was converted to a single Conv-3 for inference.

shells discarded in center cropping (see Fig.6). We used the same padding method in the convolutional and upscale paths, with the exception of `zero-repl` and `zero-zero` where the latter designator signifies the upscale padding method. The upscale output was cropped identically to output crop, rendering `zero-repl` and `zero-zero` equivalent (denoted `zero`) for output crop ≥ 1 .

We used a dataset of 10k 512×512 pixel Sentinel 2 Level-1C RGB images (Niemitalo et al. 2024). We linearly mapped reflectances 0 to 1 to values -1 to 1. We split the data to a training set of 9k images and a test set of 1k images. The mean over images and channels of the variance of the test set was 0.44 with RGB means -0.28, -0.31, and -0.22. To assemble a training batch we randomly picked images without replacement from the set, randomly cropped each image to 200×200 , created a low-resolution version by bilinearly downscaling with anti-aliasing to 50×50 , and center cropped the images to remove edge effects resulting in 192×192 target images and 48×48 input images.

We used a batch size of 64 and the Adam optimizer (Kingma 2014) with $\varepsilon = 10^{-3}$ (increased to improve stability) and default $b_1 = 0.9$ and $b_2 = 0.999$, and learning rate linearly ramped from 5×10^{-6} to 0.014 over steps 0 to 100 (warmup, tuned for a low failure rate without sacrificing learning rate much) and from 0.014 to 0 over steps 1M to 1.5M (cooldown). We repeated the training with up to 12 different random number generator seeds.

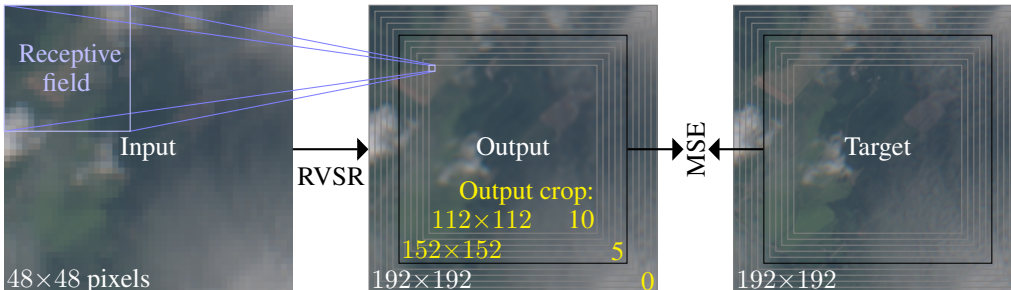


Figure 6: Illustration of RVSR super-resolution output cropping in MSE calculation, showing output crop 5 as an example. At output crop 10, the theoretical receptive fields do not include any padding.

For trained models, we also evaluated test MSE separately for shells #0–10, including in shell #10 also the rest of the shift-equivariantly processed output center. We report bootstrapped 95% confidence intervals over seeds for mean MSE and mean relative MSE difference. Test loss was calculated using center-cropped dataset images during training and by cropping at each corner in final evaluation.

Each training run took ~ 4 days on a single NVIDIA V100 32G GPU, ~ 2.5 GPU years in total consuming ~ 5 MWh of 100% renewable energy. Development and testing consumed $\sim 15\%$ additional compute. We used a V100S 32G to evaluate final MSEs, and an RTX 4070 Ti 16G for maximum batch size binary search and GPU throughput measurement at maximum batch size.

| Output crop | Conv and upscale padding method(s) | FFT (\mathcal{F}) or direct (D) autocorrelation | Maximum training batch size (images) \uparrow | Training throughput (images/s) \uparrow | Maximum inference batch size (images) \uparrow | Inference throughput (10^6 pixels/s) \uparrow | Mean test MSE (10^{-6}) \downarrow | Mean test MSE diff to zero-repl (%) \downarrow | Outermost shell mean test MSE diff to zero-repl (%) \downarrow |
|-------------|------------------------------------|---|---|---|--|--|--|--|--|
| 0 | extr1 | | 266 | 480 | 6741 | 865 | 545.0 ± 2.4 | -0.25 ± 0.31 | 0.43 ± 0.24 |
| | extr2 | | 266 | 480 | 6741 | 759 | 550.5 ± 2.9 | 0.77 ± 0.35 | 5.67 ± 0.53 |
| | extr3 | | 266 | 478 | 6741 | 758 | 559.6 ± 1.9 | 2.38 ± 0.39 | 11.98 ± 0.40 |
| | lp1x1cs | | 237 | 464 | 6741 | 722 | 543.3 ± 3.3 | -0.64 ± 0.39 | -1.82 ± 0.28 |
| | lp2x1 | D | 190 | 433 | 6741 | 498 | 543.2 ± 2.3 | -0.63 ± 0.25 | -1.71 ± 0.19 |
| | lp2x1cs | | 189 | 442 | 6741 | 632 | 542.9 ± 2.9 | -0.68 ± 0.28 | -1.88 ± 0.14 |
| | lp2x3 | D | 187 | 429 | 6741 | 480 | 542.8 ± 3.0 | -0.71 ± 0.19 | -1.90 ± 0.18 |
| | lp2x5 | \mathcal{F} | 240 | 453 | 6020 | 382 | 542.7 ± 2.5 | -0.72 ± 0.17 | -1.90 ± 0.11 |
| | lp3x3 | \mathcal{F} | 241 | 455 | 6020 | 394 | 543.2 ± 2.5 | -0.65 ± 0.25 | -1.89 ± 0.12 |
| | lp4x5 | \mathcal{F} | 236 | 447 | 6020 | 356 | 543.2 ± 3.5 | -0.63 ± 0.39 | -1.77 ± 0.18 |
| | lp6x7 | \mathcal{F} | 191 | 432 | 6020 | 266 | 543.7 ± 1.8 | -0.49 ± 0.23 | -1.34 ± 0.23 |
| | repl | | 266 | 481 | 6880 | 870 | 544.6 ± 3.1 | -0.39 ± 0.30 | 0.28 ± 0.17 |
| | zero-repl | | 263 | 472 | 6880 | 964 | 546.6 ± 1.9 | 0.00 | 0.00 |
| zero-zero | | 263 | 472 | 6741 | 960 | 547.1 ± 1.8 | 0.09 ± 0.26 | 1.32 ± 0.15 | |
| 1 | lp1x1cs | | 238 | 468 | 7314 | 695 | 532.2 ± 1.6 | -0.27 ± 0.29 | -0.93 ± 0.16 |
| | lp2x1cs | | 191 | 444 | 7314 | 608 | 532.0 ± 1.8 | -0.27 ± 0.17 | -0.88 ± 0.20 |
| | lp2x3 | D | 188 | 436 | 7314 | 473 | 532.5 ± 2.3 | -0.22 ± 0.26 | -0.88 ± 0.13 |
| | repl | | 268 | 481 | 7314 | 808 | 532.8 ± 2.6 | -0.16 ± 0.31 | -0.07 ± 0.13 |
| | zero | | 268 | 483 | 7314 | 896 | 533.6 ± 2.0 | 0.00 | 0.00 |
| 5 | lp2x3 | D | 257 | 486 | 8403 | 465 | 531.8 ± 2.8 | -0.05 ± 0.30 | -0.16 ± 0.14 |
| | repl | | 325 | 518 | 8403 | 664 | 531.7 ± 2.5 | -0.06 ± 0.27 | -0.14 ± 0.17 |
| | zero | | 325 | 518 | 8403 | 706 | 532.0 ± 2.2 | 0.00 | 0.00 |

Table 1: RVSR evaluation results. 95% confidence intervals are reported (gray means lack of data).

4 Results and discussion

For sample images padded using variants of 1p and other methods, see Appendix B. In RVSR super-resolution training, we observed catastrophic Adam optimizer instability with some seed-method combinations (see Appendix D). We believe that this was a chaotic effect due to both a high learning rate and to numerical issues exemplified by differences between the equivalent `repl` and `extr1`, and not indicative of an inherent difference in training stability between the various padding methods. Overall training dynamics (Fig. 9) were similar between the padding methods, with the exception of lower early-training test MSE for `repl` and the 1p methods, compared to a `zero-repl` baseline, when trained without output crop. The main evaluation results for trained models can be found in Table 1, and sample images and a visualization of the deviation from shift equivariance in Appendix E.

The different 1p methods yielded very similar super-resolution test MSEs, bringing the light-weight `lp1x1cs` and `lp2x1cs` to the inference throughput–MSE Pareto front (see Fig. 10) for each output crop 0 and 1. The 1p methods that used FFT-accelerated autocorrelation reached larger batch sizes in training but were limited to smaller batch sizes in inference, in comparison to 1p methods that calculated autocorrelation directly and used a similar neighborhood size.

For output crop 0, every tested 1p method yielded a 0.20–0.9% (at 95% confidence) lower mean test MSE and 1.5–2.0% lower outermost shell mean test MSE compared to the standard `zero-repl` baseline (see Tab. 1). For the other shells (see Fig. 7), `lp2x3` and `repl` were tied but consistently better than the baseline. Compared to the baseline, `repl` improved the test mean MSE by 0.1–0.7% but, notably, was 0.1–0.5% worse at the outermost shell. We hypothesize that the more clear

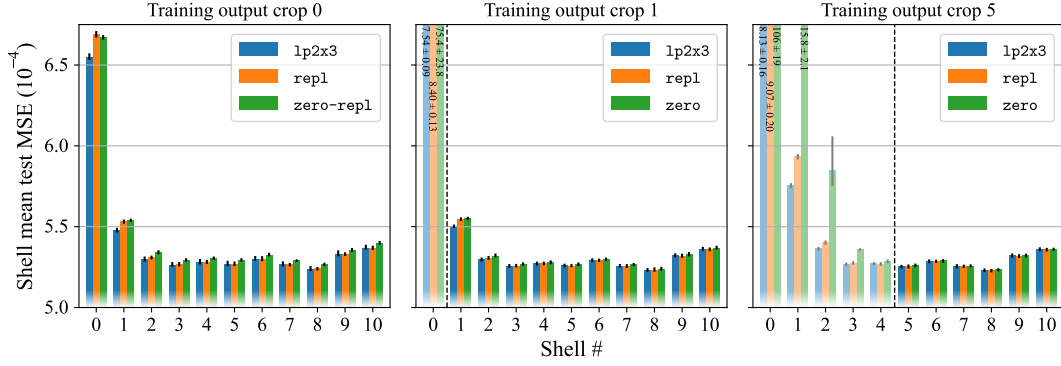


Figure 7: Super-resolution mean test MSE for select models, calculated separately for shells of equivalent width of 1 input pixel (bounded by squares in Fig. 6). Error bars indicate 95% confidence interval of the mean. Results for each output crop only include those seeds for which training was successful for every method listed. Pale-colored bars indicate exclusion of shells from training loss.

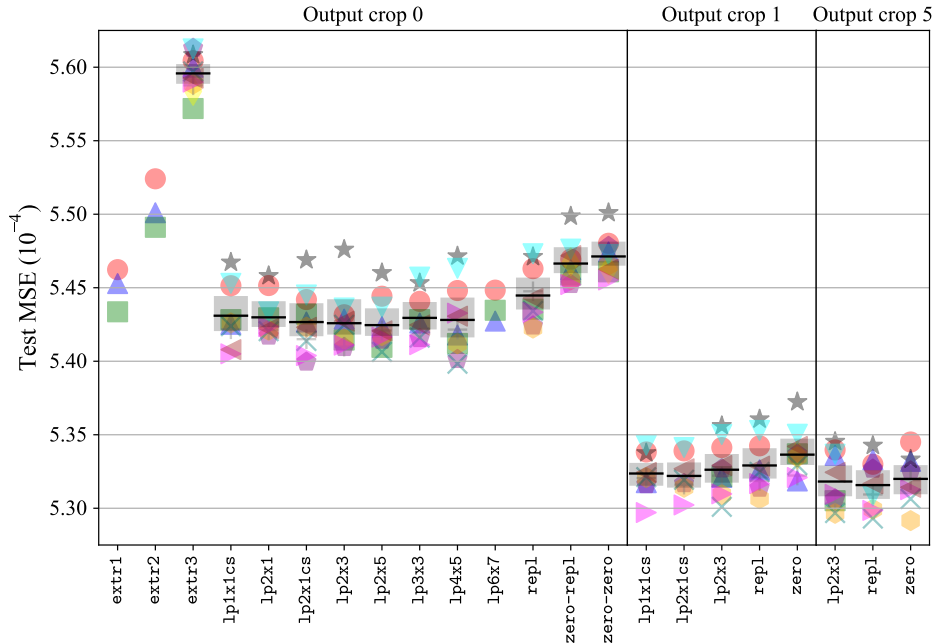


Figure 8: Super-resolution test MSE with mean (—) and the 95% confidence interval of the mean (■) across all successful training runs. For seed values, see Appendix D.

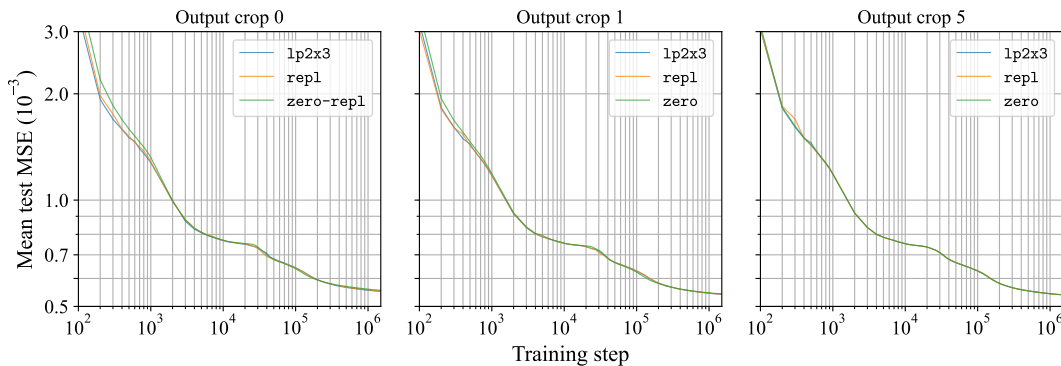


Figure 9: Super-resolution mean test loss during training for select padding methods, including for each output crop only those seeds that resulted in a successful training run for every method listed.

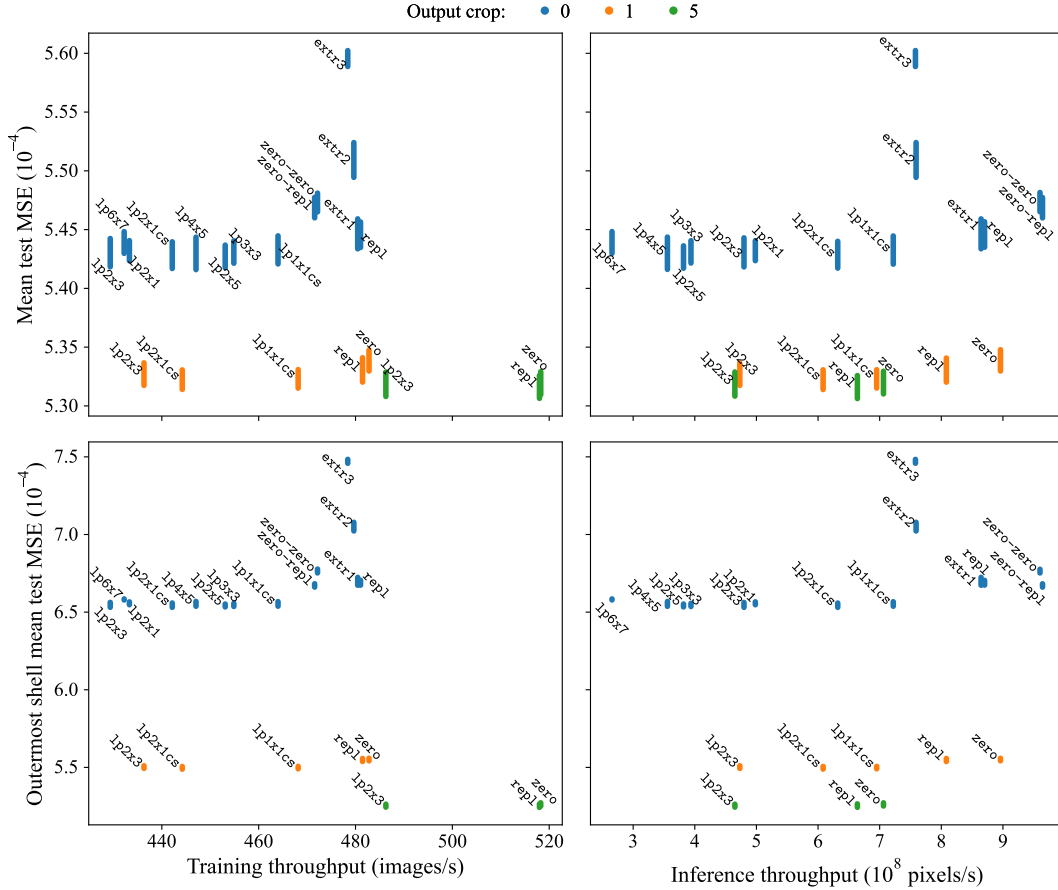


Figure 10: 95% confidence interval of the mean super-resolution MSE of each model vs. training/inference throughput evaluated using maximum training/inference batch sizes. Except for the outermost shell mean test MSE, the results do not apply to other than the used 48×48 pixel input image size because of the difference in the ratio of output pixels influenced by padding.

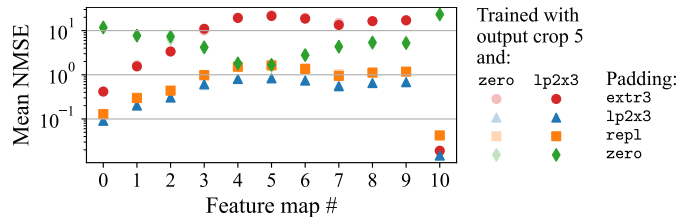


Figure 11: Test mean-over-seeds NMSE (MSE divided by data variance) of padding each convolution layer input (low-res input #0 and feature maps #1–9) and high-res network output (#10) from a 28×28 -pixel center crop to 30×30 pixels, in a trained RVSR network. Padding by mean would give $\text{NMSE} = 1$. Sparsity differences (Aimar et al. 2018) may contribute to predictability differences.

edge signal and worse data approximation by zero-repl, compared to repl, enables and forces the network to use some of its capacity to improve shell #0 performance at the cost of overall performance. As an approximator of the internal feature maps of a trained RVSR network (with GELU activation), zero has up to 40-fold larger error than repl and lp2x3 (see Fig. 11). The worse approximation by zero is illustrated by the up to 10-fold MSE error growth for shells not included in the training loss and outside the output crop (shaded gray in Fig. 7), compared to repl and lp2x3. Compared to explicit zero, the default implicit repl in bilinear upscale gave a lower outermost shell mean test MSE.

For output crop 1, the choice of padding method mattered less, with `1p2x3` improving upon the baseline at the two outermost shells. Models trained with output crop 5 saw no difference from the choice of padding method. Furthermore, the test MSEs have only relatively modest differences between output crops. At shells $\# \geq 5$, all models perform similarly with the exception of the somewhat worse output crop 0 `zero-repl`. This might be because training with output crop doesn't free up sufficient capacity to decrease MSE in the remaining image area for `repl` and `1p2x3`.

For `extr N` we found test MSE to increase with N , with `extr3` giving 11–12% worse outermost shell mean MSE compared to baseline. In contrast, Leng and Thiyagalingam 2023a found the equivalent of `extr3` (see GitHub issue #2 in Leng and Thiyagalingam 2023b for a numerical demonstration of equivalence) to give better results in a U-net super-resolution task than `zero` or `repl`, which we suspect was due to their use of blurred inputs (Gaussian blur of standard deviation $\sigma = 3$) that are better approximated by the higher-degree `extr3` method (see Appendix C).

5 Conclusions

Using linear prediction padding (`1p`) instead of `zero` or replication padding (`repl`) improved slightly the quality of CNN-based super-resolution, in particular near image borders, at a moderate added time cost. Center-cropping the network output leveled the differences in output–target mean square error between padding methods. At output crop 5 the stitching artifacts due to deviation from shift equivariance were no longer visible.

Considering padding as autoregressive estimation of data and feature maps explains some of the differences between padding methods. However, the tested CNN architecture learned to compensate the elevated super-resolution error near the image edge to roughly the same magnitude for all the tested padding methods, including `zero` which has an exceptionally high estimation error. The slightly higher overall super-resolution error with `zero` supports the hypothesis that more network capacity is consumed by the compensation of the larger padding error.

Our results might not directly apply to other CNN architectures and tasks. Covariance statistics may suffer from the small sample problem with spatially tiny inputs such as encodings. Larger effective receptive fields may favor `1p`, whereas workloads with a higher level of spatial inhomogeneity, lower spatial correlations in network input or feature maps (in particular spatially whitened data), or higher nonlinearity in spatial dependencies would likely make `1p` less useful, favoring `zero` for its clear edge signaling. If using `1p` in CNN-based processing of images with *framing*, for example photos of objects, any needed location information might need to come from another source than the padding.

Our JAX `1p` padding implementation and source code for reproducing the results of this article are freely available (Rosenberg and Niemitalo 2025). Our `1p1x1cs` and `1p2x1cs` methods would be the most straightforward ones to port to other frameworks.

6 Further work

We have yet to explore 1) using a spatially weighted loss to level spatial differences in error, 2) using batch rather than image statistics for a larger statistical sample, 3) increasing the sample size by giving `1p` memory of past statistics, 4) learning rather than solving `1p` coefficients, 5) modeling dependencies between channels, 6) instead of output cropping, cross-fading adjacent output tiles and optimizing the cross-fade curves during training, 7) setting the padding method separately for each feature map based on its spatial autocorrelation, 8) accelerating solves by taking advantage of the covariance matrix structure, and 9) use of `1p` in other CNN architectures and training settings.

7 Contributions and acknowledgements

The article was written by Olli Niemitalo (who wrote the theory) and Otto Rosenberg, and reviewed by Nathaniel Narra and Iivari Kunttu. Implementations were written by Otto Rosenberg and Olli Niemitalo. The work was supervised by Olli Koskela and Iivari Kunttu. The work was supported by the Research Council of Finland funding decision 353076, Digital solutions to foster climate-smart agricultural transition (Digi4CSA). Model training was done on the CSC – IT Center for Science, Finland supercomputer Puhti. The dataset used contains Copernicus Sentinel data 2015–2022.

References

- Alessandro Aimar, Hesham Mostafa, Enrico Calabrese, Antonio Rios-Navarro, Ricardo Tapiador-Morales, Iulia-Alexandra Lungu, Moritz B Milde, Federico Corradi, Alejandro Linares-Barranco, Shih-Chii Liu, et al. NullHop: A flexible convolutional neural network accelerator based on sparse representations of feature maps. *IEEE transactions on neural networks and learning systems*, 30(3):644–656, 2018.
- Andre Araujo, Wade Norris, and Jack Sim. Computing receptive fields of convolutional neural networks. *Distill*, 2019. doi: 10.23915/distill.00021. <https://distill.pub/2019/computing-receptive-fields>.
- James Bradbury, Roy Frostig, Peter Hawkins, Matthew James Johnson, Chris Leary, Dougal Maclaurin, George Necula, Adam Paszke, Jake VanderPlas, Skye Wanderman-Milne, and Qiao Zhang. JAX: composable transformations of Python+NumPy programs, 2025. URL <http://github.com/jax-ml/jax>.
- Marcos V. Conde, Zhijun Lei, Wen Li, Cosmin Stejerean, Ioannis Katsavounidis, Radu Timofte, Kihwan Yoon, Ganzorig Gankhuyag, Jiangtao Lv, Long Sun, Jinshan Pan, Jiangxin Dong, Jinhui Tang, Zhiyuan Li, Hao Wei, Chenyang Ge, Dongyang Zhang, Tianle Liu, Huaian Chen, Yi Jin, Menghan Zhou, Yiqiang Yan, Si Gao, Biao Wu, Shaoli Liu, Chengjian Zheng, Diankai Zhang, Ning Wang, Xintao Qiu, Yuanbo Zhou, Kongxian Wu, Xinwei Dai, Hui Tang, Wei Deng, Qingquan Gao, Tong Tong, Jae-Hyeon Lee, Ui-Jin Choi, Min Yan, Xin Liu, Qian Wang, Xiaoqian Ye, Zhan Du, Tiansen Zhang, Long Peng, Jiaming Guo, Xin Di, Bohao Liao, Zhibo Du, Peize Xia, Renjing Pei, Yang Wang, Yang Cao, Zhengjun Zha, Bingnan Han, Hongyuan Yu, Zhuoyuan Wu, Cheng Wan, Yuqing Liu, Haodong Yu, Jizhe Li, Zhijuan Huang, Yuan Huang, Yajun Zou, Xianyu Guan, Qi Jia, Heng Zhang, Xuanwu Yin, Kunlong Zuo, Hyeon-Cheol Moon, Tae hyun Jeong, Yoonmo Yang, Jae-Gon Kim, Jinwoo Jeong, and Sunjei Kim. Real-time 4k super-resolution of compressed AVIF images. AIS 2024 challenge survey, 2024. URL <https://arxiv.org/abs/2404.16484>.
- Bohao Huang, Daniel Reichman, Leslie M Collins, Kyle Bradbury, and Jordan M Malof. Tiling and stitching segmentation output for remote sensing: Basic challenges and recommendations. *arXiv preprint arXiv:1805.12219*, 2018.
- Patrick Kidger and Cristian Garcia. Equinox: neural networks in JAX via callable PyTrees and filtered transformations. *Differentiable Programming workshop at Neural Information Processing Systems 2021*, 2021.
- Diederik P Kingma. Adam: A method for stochastic optimization. *arXiv preprint arXiv:1412.6980*, 2014.
- Kuangdai Leng and Jeyan Thiyagalingam. Padding-free convolution based on preservation of differential characteristics of kernels, 2023a. URL <https://arxiv.org/abs/2309.06370>.
- Kuangdai Leng and Jeyan Thiyagalingam. DiffConv2d GitHub repository, 2023b. URL <https://github.com/stfc-sciml/DifferentialConv2d>.
- Wenjie Luo, Yujia Li, Raquel Urtasun, and Richard Zemel. Understanding the effective receptive field in deep convolutional neural networks. *Advances in neural information processing systems*, 29, 2016.
- John Makhoul. Linear prediction: A tutorial review. *Proceedings of the IEEE*, 63(4):561–580, 1975.
- Olli Niemitalo, Elias Anzini, Jr, and Vinicius Hermann D. Liczkoski. 10k random 512x512 pixel Sentinel 2 Level-1C RGB satellite images over Finland, years 2015–2022. <https://doi.org/10.23729/32a321ac-9012-4f17-a849-a4e7ed6b6c8c>, 10 2024. HAMK Häme University of Applied Sciences.
- Jason Rader, Terry Lyons, and Patrick Kidger. Lineax: unified linear solves and linear least-squares in JAX and Equinox. *AI for science workshop at Neural Information Processing Systems 2023*, *arXiv:2311.17283*, 2023.
- Otto Rosenberg and Olli Niemitalo. hamk-uas/linear-prediction-padding-paper: v1, February 2025. URL <https://doi.org/10.5281/zenodo.14871260>.

A Stabilization of 1D covariance method linear prediction

For 1D linear prediction neighborhoods 1×1 (stabilized covariance method $1p1x1cs$) and 2×1 ($1p2x1cs$), the padding procedure in one direction (Eq. 4) using already calculated coefficients $a_{1\dots P}$ is equivalent to a discrete-time linear time-invariant (LTI) system having a causal recursion:

$$1 \times 1: y[k] = a_1 y[k-1] + b_0 x[k], \quad 2 \times 1: y[k] = a_1 y[k-1] + a_2 y[k-2] + b_0 x[k], \quad (11)$$

where $y[k]$ are known pixel values or padding pixels, $x[k]$ are input pixels with $x[k] = 0$ for all k with an inconsequential input coefficient b_0 . The corresponding transfer functions are:

$$\begin{aligned} 1 \times 1: \quad H(z) &= \frac{b_0}{1 - a_1 z^{-1}} \\ &= \frac{b_0 z}{z - p_0}, \\ p_0 &= a_1 \end{aligned} \quad \begin{aligned} 2 \times 1: \quad H(z) &= \frac{b_0}{1 - a_1 z^{-1} - a_2 z^{-2}} \\ &= \frac{b_0 z^2}{(z - p_0)(z - p_1)}, \\ p_0 &= \frac{a_1 + \sqrt{a_1^2 + 4a_2}}{2} \\ p_1 &= \frac{a_1 - \sqrt{a_1^2 + 4a_2}}{2}, \end{aligned} \quad (12)$$

where b_0 is an input scaling factor, z^{-1} represents a delay of one sampling period, and $H(e^{i\omega})$, represents the frequency response of the system with ω the frequency in radians per sampling period, e the natural number, and i the imaginary unit.

The system is stable if all poles p of the transfer function lie inside the complex z -plane unit circle. A stationary autoregressive process is stable. If the coefficients were found by solving normal equations with approximate covariances, then stability is not guaranteed. In practice, stability is needed to prevent blow-up of the padding output when padding recursively.

By reciprocating the z -plane radius of all poles that have radius > 1 , the system can be made stable, or marginally stable in case any of the poles lie at radius 1 exactly. An unstable system has no well-defined frequency response, but we can still compute $H(e^{i\omega})$. The stabilization alters the phase of $H(e^{i\omega})$ but maintains its magnitude up to a constant scaling factor that is inconsequential with zero input, thus preserving the essential power-spectral characteristics of the autoregressive process. Magnitude scaling could be compensated for by setting $b'_0 = b_0(1 - \sum_{i=0}^{i < P} a'_i) / (1 - \sum_{i=0}^{i < P} a_i)$ where $'$ denotes updated variables. The choice of b_0 is inconsequential with constant zero input but would matter in *generative* padding with x a white noise *innovation*.

For a 2×1 neighborhood, if what's under the square root in Eq. 12 is negative, $a_1^2 + 4a_2 < 0$, then the poles are complex and form a complex conjugate pair. Otherwise, both poles are real. The squared magnitudes of the complex conjugate pair of poles are equal, $|p_0|^2 = |p_1|^2 = -a_2$. The complex poles lie outside the unit circle only if $-a_2 > 1$, in which case the system can be stabilized by $a'_1 = -a_1/a_2$, $a'_2 = 1/a_1$. Real poles p_0 and p_1 can be found using Eq. 12, they can be reciprocated when necessary, and the modified coefficients can be extracted from the expanded form of the numerator polynomial as: $a'_1 = p'_0 + p'_1$ and $a'_2 = p'_0 p'_1$.

The characteristic polynomial of the AR process is the denominator of the transfer function Eq. 12 written with lag operator $B = z^{-1}$. With the characteristic polynomial the stability condition is that all roots are outside the unit circle. Stabilization via the characteristic polynomial would manipulate the coefficients identically to what was presented above.

B Sample padded images

Fig. 12 shows sample padded images. For information about the image dataset, see section 3.

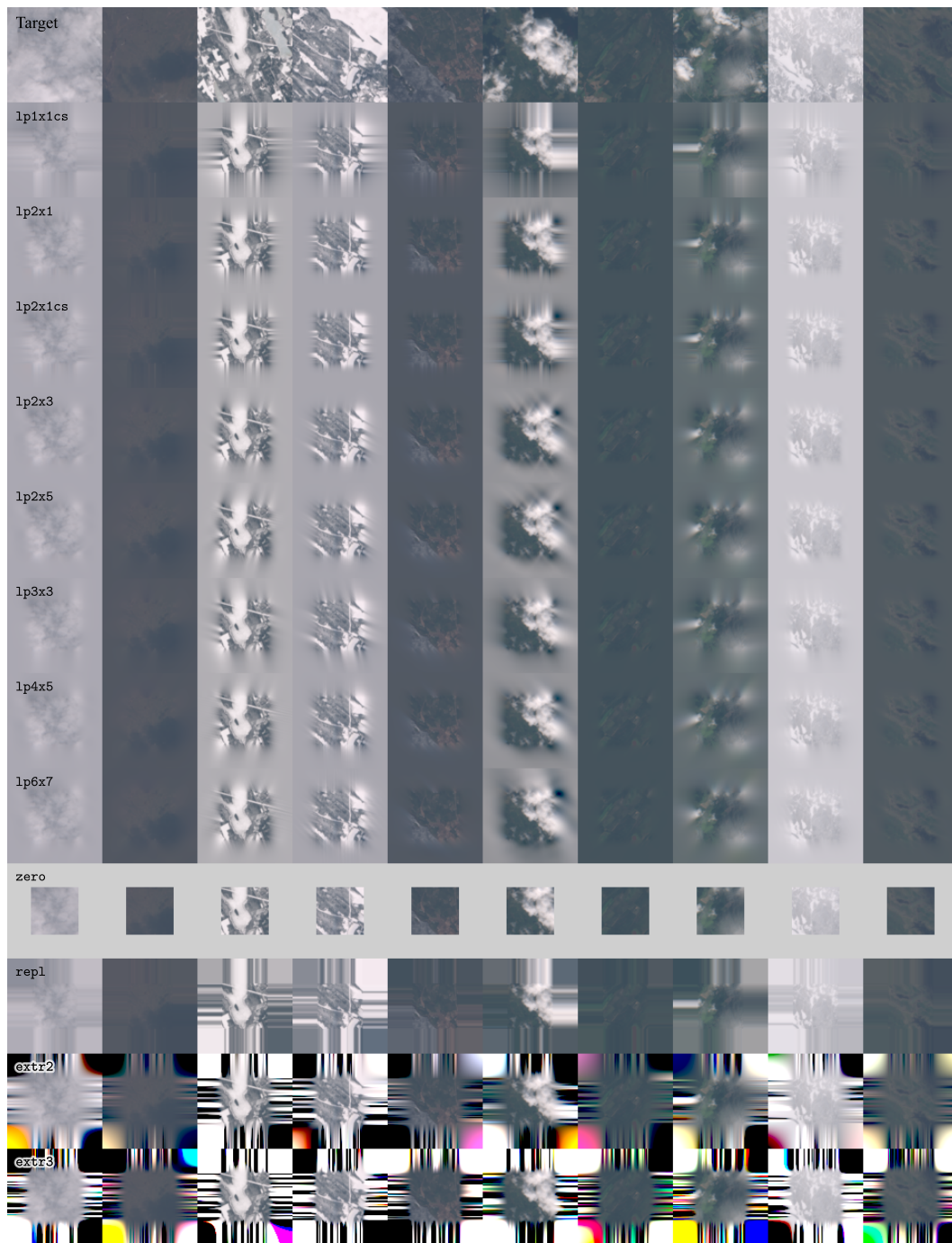


Figure 12: Non-cherry-picked 48×48 pixel test set satellite images padded with 24 pixels on each side, using different methods. The first row shows the ground truth (*target*) image from which each padding input was center-cropped (see the *zero* row for the crop boundaries). The 1p methods with larger neighborhood widths capture directional regularities with larger slopes off the padding direction. The *extr2* and *extr3* recursions are unstable. Color channels have been clipped to reflectance range 0–0.8.

C Effect of blur on padding error

To simulate padding input data having an adjustable degree of blurriness or a rate of frequency spectral decay, we model Gaussian-blurred white-noise data by uniformly sampling a zero-mean Gaussian process x of unit variance and with Gaussian covariance as function of lag d :

$$\text{Cov}(x[i], x[i + d]) = \kappa(d) = \exp\left(-\frac{d^2}{2\sigma^2}\right) \quad \text{for all integer } i, \quad (13)$$

with σ corresponding to the standard deviation of the Gaussian blur. A general linear right padding method approximates $x[0]$ from the P nearest samples by $\hat{x}[0] = \sum_{i=1}^P a_i x[-i]$. We define the padding error ε with the sign convention:

$$\varepsilon = \hat{x}[0] - x[0] = \sum_{i=0}^P a_i x[-i], \quad a_0 = -1, \quad (14)$$

prepending $a_{1\dots P}$ with $a_0 = -1$ for convenience. The normalized mean square of the zero-mean ε is:

$$\text{NMSE} = \frac{\text{E}(\varepsilon^2)}{\text{Var}(x)} = \frac{\text{Var}(\varepsilon)}{1} = \sum_{i=0}^P \sum_{j=0}^P \text{Cov}(a_i x[-i], a_j x[-j]) = \sum_{i=0}^P \sum_{j=0}^P a_i a_j \kappa(j - i) \quad (15)$$

We compare in Fig. 13 the MSE for the following 1D padding methods with some equivalencies:

| Method(s) | P | $a_{0\dots P}$ |
|----------------|-----|---------------------|
| zero, extr0 | 0 | -1 |
| repl, extr1 | 1 | -1, 1 |
| extr2 | 2 | -1, 2, -1 |
| extr3 | 3 | -1, 3, -3, 1 |
| lp1x1cs | 1 | -1, a_1 |
| lp2x1, lp2x1cs | 2 | -1, a_1, a_2 |
| lp3x1 | 3 | -1, a_1, a_2, a_3 |

(16)

with $a_{1\dots P}$ for lp1x1cs, lp2x1, and lp2x1cs from Eq. 7 and for lp3x1 from solving Eq. 8 using Levinson recursion, with known autocorrelation-like covariances $r_{ij} = \kappa(j - i)$, corresponding to the limiting case of infinitely vast padding input providing covariance statistics matching the covariances of the Gaussian process.

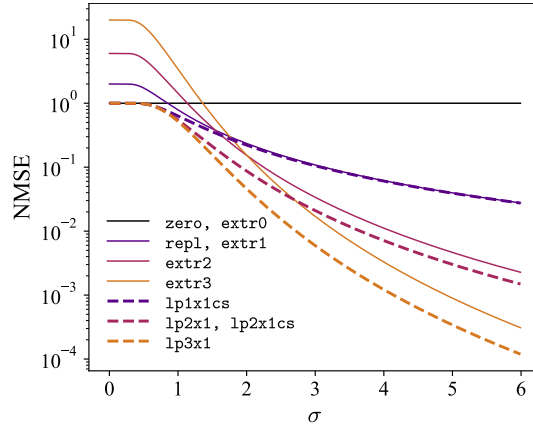


Figure 13: Theoretical padding NMSE as function of standard deviation σ of Gaussian blur applied to white-noise data. Padding input is the blurred data normalized to unit variance. Increasing the order of the extr padding mode increases the error for low σ and decreases it for high σ . Each lp method has been least-squares fit to the known signal model and thus attains the lowest possible MSE given the number of predictors. zero remains ideal for data with zero autocorrelation at non-zero lags.

D Trained models

| output crop | padding method | seed / symbol | | | | | | | | | | | |
|-------------|----------------|---------------|---|---|---|---|---|---|---|---|---|----|----|
| | | 0 | 1 | 2 | 3 | 4 | 5 | 6 | 7 | 8 | 9 | 10 | 11 |
| 0 | lp1x1cs | ✓ | ✓ | ✓ | ✗ | ✗ | ✓ | ✓ | ✓ | ✓ | ✓ | ✓ | ✓ |
| | lp2x1 | ✓ | ✗ | ✓ | ✗ | ✓ | ✓ | ✓ | ✓ | ✓ | ✓ | ✓ | ✓ |
| | lp2x1cs | ✓ | ✓ | ✓ | ✗ | ✓ | ✓ | ✓ | ✓ | ✓ | ✓ | ✓ | ✓ |
| | lp2x3 | ✓ | ✓ | ✓ | ✗ | ✓ | ✓ | ✓ | ✓ | ✓ | ✓ | ✓ | ✓ |
| | lp2x5 | ✓ | ✓ | ✓ | ✗ | ✓ | ✓ | ✓ | ✓ | ✓ | ✓ | ✓ | ✓ |
| | lp3x3 | ✓ | ✓ | ✓ | ✗ | ✓ | ✗ | ✓ | ✓ | ✓ | ✓ | ✓ | ✓ |
| | lp4x5 | ✓ | ✓ | ✓ | ✗ | ✓ | ✓ | ✓ | ✓ | ✓ | ✓ | ✓ | ✓ |
| | lp6x7 | ✓ | ✓ | ✓ | — | — | — | — | — | — | — | — | — |
| | zero-repl | ✓ | ✓ | ✓ | ✓ | ✓ | ✓ | ✓ | ✗ | ✗ | ✓ | ✓ | ✓ |
| | zero-zero | ✓ | ✓ | ✓ | ✓ | ✓ | ✓ | ✓ | ✗ | ✗ | ✓ | ✓ | ✓ |
| | repl | ✓ | ✗ | ✓ | ✗ | ✓ | ✓ | ✓ | ✓ | ✓ | ✓ | ✓ | ✓ |
| | extr1 | ✓ | ✓ | ✓ | — | — | — | — | — | — | — | — | — |
| | extr2 | ✓ | ✓ | ✓ | — | — | — | — | — | — | — | — | — |
| | extr3 | ✓ | ✓ | ✓ | ✓ | ✓ | ✓ | ✓ | ✓ | ✓ | ✓ | ✓ | ✓ |
| 1 | lp1x1cs | ✓ | ✓ | ✗ | ✗ | ✓ | ✓ | ✓ | ✓ | ✓ | ✓ | ✓ | |
| | lp2x1cs | ✓ | ✗ | ✗ | ✗ | ✓ | ✓ | ✗ | ✓ | ✓ | ✓ | ✓ | |
| | lp2x3 | ✓ | ✓ | ✓ | ✗ | ✓ | ✓ | ✓ | ✓ | ✓ | ✓ | ✓ | |
| | zero | ✗ | ✓ | ✓ | ✓ | ✓ | ✓ | ✓ | ✓ | ✓ | ✓ | ✓ | |
| | repl | ✓ | ✓ | ✗ | ✗ | ✓ | ✓ | ✓ | ✓ | ✓ | ✓ | ✓ | |
| 5 | lp2x3 | ✓ | ✓ | ✓ | ✗ | ✓ | ✓ | ✓ | ✓ | ✓ | ✓ | ✓ | |
| | zero | ✓ | ✓ | ✗ | ✗ | ✓ | ✓ | ✓ | ✓ | ✓ | ✗ | ✓ | |
| | repl | ✓ | ✓ | ✗ | ✗ | ✓ | ✓ | ✓ | ✓ | ✓ | ✓ | ✓ | |

Super-resolution training was either successful (✓), failed (✗), or skipped (—) for different combinations of padding methods and the random number generator seed. We report loss differences between models using only seeds that resulted in successful training for both of the compared models.

E Tiled processing samples and deviation from shift equivariance

Figs. 15–17 show non-cherry-picked stitched tiled processing results from models trained with seed 10, using different output crops. Fig. 14 show the corresponding inputs and targets from the test set. Figs. 18–20 visualize deviation from shift equivariance for the same images.



Figure 14: The super-resolution inputs and targets from the test set, cropped to the same view as the sample results.

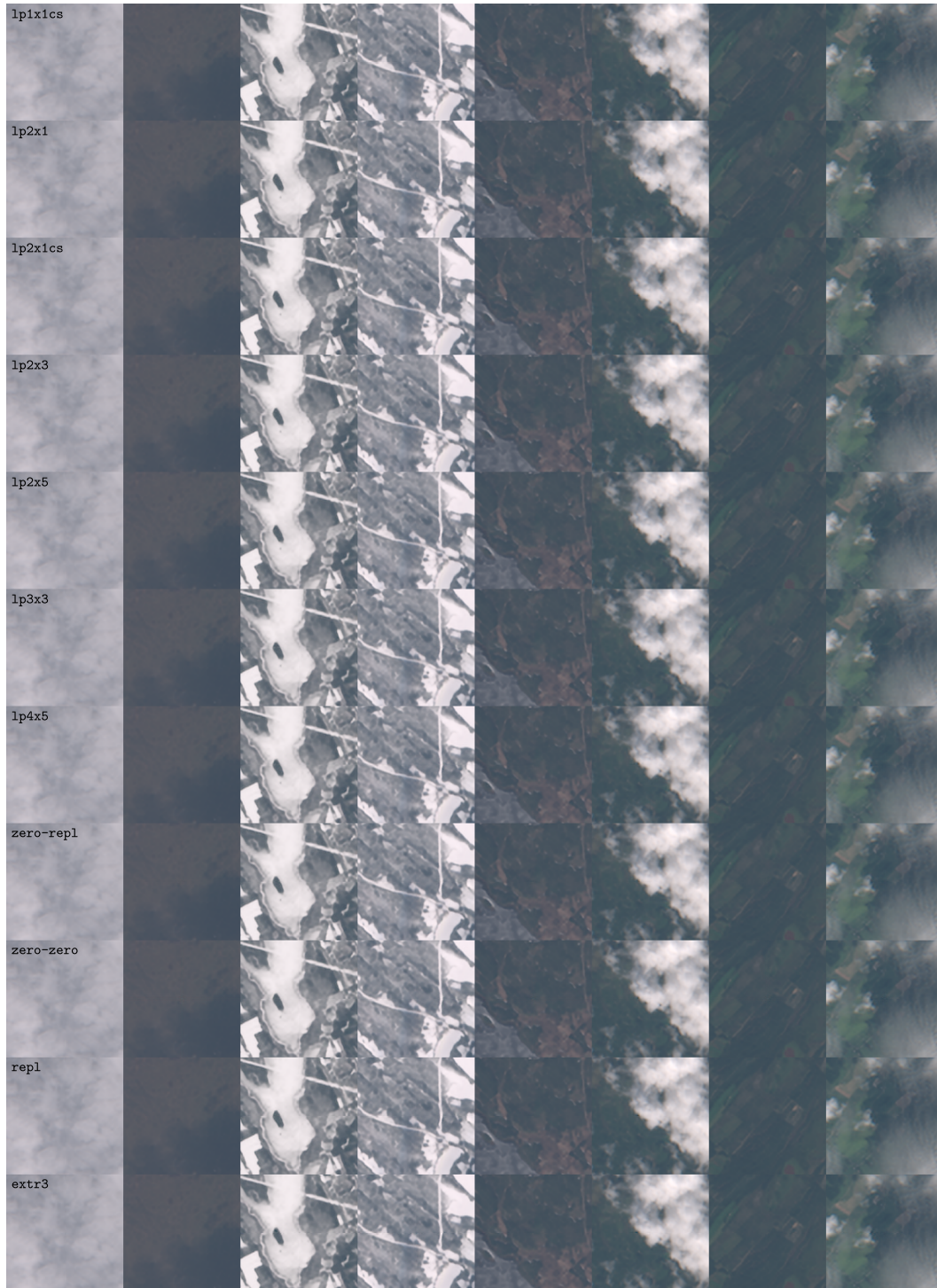


Figure 15: Stitched RVSr super-resolution results with output crop 0. Four output tiles, each as large as the images shown, were stitched together with a corner of the tiling grid at the center of each image. A cross-hair-shaped discontinuity artifact is formed due to deviation from shift equivariance. Black represents zero reflectance and white represents a reflectance of 0.8 on every channel.



Figure 16: Stitched RVSr super-resolution results with output crop 1. Visually, the discontinuity artifact is much weaker than with output crop 1 and is only visible on high-contrast edges not perpendicular to the tile boundary.

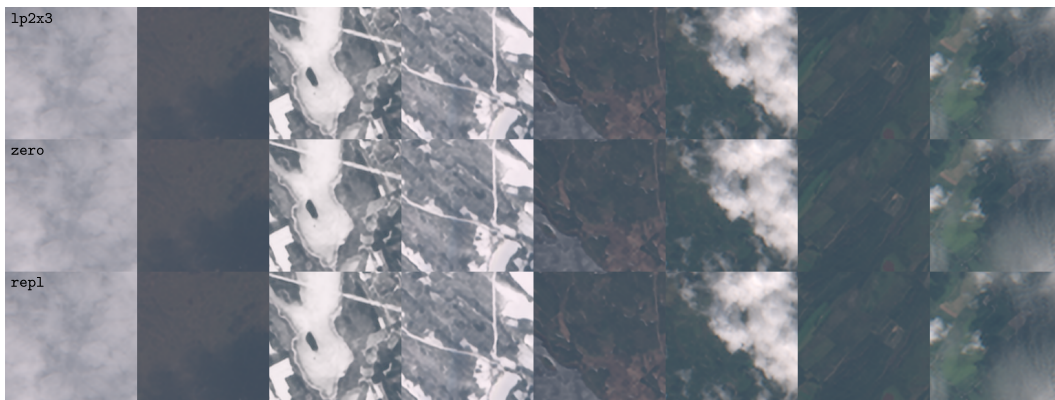


Figure 17: Stitched RVSr super-resolution results with output crop 5. No visible tiling artifacts.

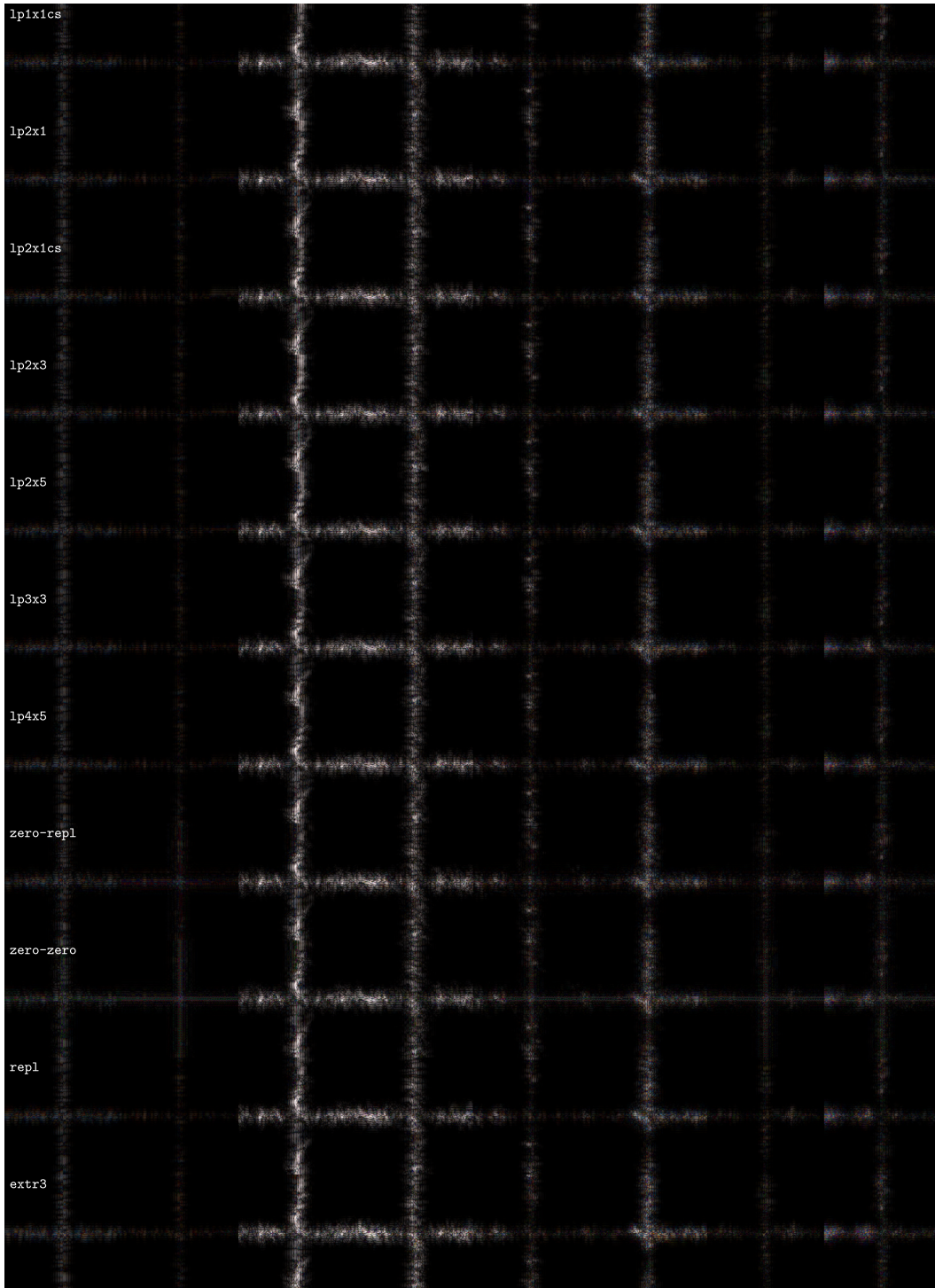


Figure 18: RVSR super-resolution deviation from shift equivariance for output crop 0, calculated as the absolute value of the difference between a stitched tiled prediction and a prediction using only valid convolutions. Black represents no difference and white represents an absolute reflectance difference of 0.2 on every channel.

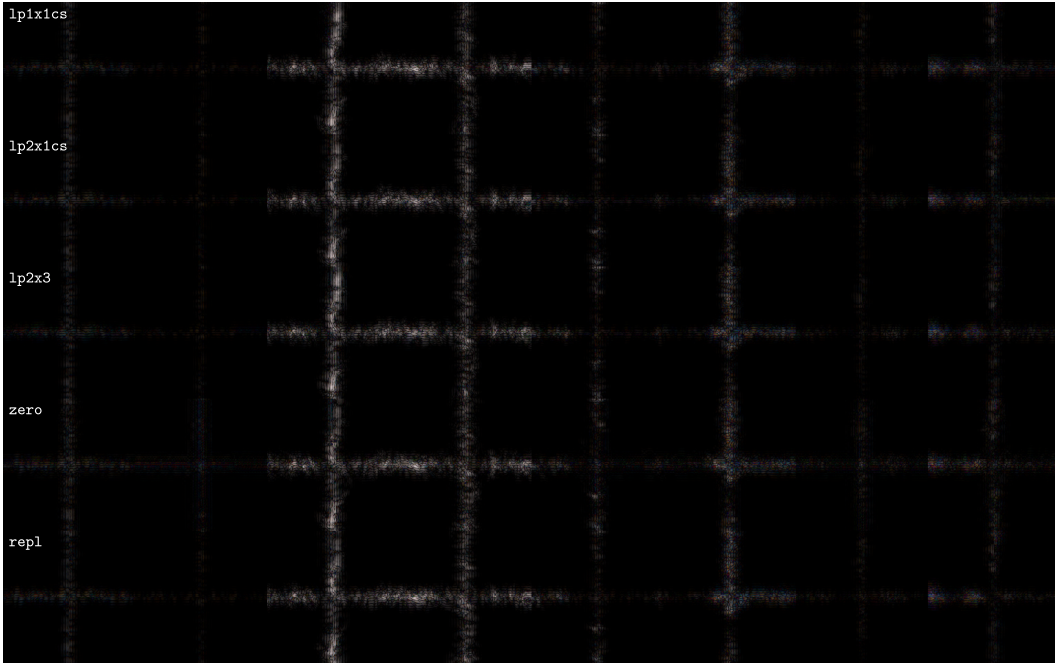


Figure 19: RCSR super-resolution deviation from shift equivariance for output crop 1.



Figure 20: RCSR super-resolution deviation from shift equivariance for output crop 5. zero displays elevated deviations compared to lp2x3 and repl.